

## Concentration and temperature dependent luminescence properties of the $\text{SrI}_2\text{-TmI}_2$ system

Plokker, M. P.; Hoogsteen, W.; Abellon, R. D.; Krämer, K. W.; van der Kolk, E.

**DOI**

[10.1016/j.jlumin.2020.117327](https://doi.org/10.1016/j.jlumin.2020.117327)

**Publication date**

2020

**Document Version**

Accepted author manuscript

**Published in**

Journal of Luminescence

**Citation (APA)**

Plokker, M. P., Hoogsteen, W., Abellon, R. D., Krämer, K. W., & van der Kolk, E. (2020). Concentration and temperature dependent luminescence properties of the  $\text{SrI}_2\text{-TmI}_2$  system. *Journal of Luminescence*, 225, Article 117327. <https://doi.org/10.1016/j.jlumin.2020.117327>

**Important note**

To cite this publication, please use the final published version (if applicable). Please check the document version above.

**Copyright**

Other than for strictly personal use, it is not permitted to download, forward or distribute the text or part of it, without the consent of the author(s) and/or copyright holder(s), unless the work is under an open content license such as Creative Commons.

**Takedown policy**

Please contact us and provide details if you believe this document breaches copyrights. We will remove access to the work immediately and investigate your claim.

# Concentration and Temperature Dependent Luminescence Properties of the $\text{SrI}_2\text{-TmI}_2$ System

M.P. Plokker<sup>a</sup>, W. Hoogsteen<sup>a</sup>, R.D. Abellon<sup>b</sup>, K.W. Krämer<sup>c</sup>, and E. van der Kolk<sup>a</sup>

<sup>a</sup>Luminescence Materials Research Group, Delft University of Technology, Mekelweg 15, 2629 JB Delft, The Netherlands

<sup>b</sup>Optoelectronic Materials Research Group, Delft University of Technology, Van der Maasweg 9, 2629 HZ Delft, The Netherlands

<sup>c</sup>Department of Chemistry and Biochemistry, University of Bern, Freiestrasse 3, 3012 Bern, Switzerland

---

## Abstract

The concentration dependent luminescence of the  $\text{SrI}_2\text{-TmI}_2$  system was investigated. For  $\text{Tm}^{2+}$  concentrations up to 5 mol %, the quantum efficiency (QE) of the  ${}^2\text{F}_{5/2} \rightarrow {}^2\text{F}_{7/2}$  emission exhibits a constant value above 50%. The QE drops for higher  $\text{Tm}^{2+}$  concentrations, partly due to concentration quenching, as evidenced by a decreasing luminescence lifetime of the  ${}^2\text{F}_{5/2} \rightarrow {}^2\text{F}_{7/2}$  emission, and partly due to the formation of a second crystal phase with  $\text{CdCl}_2$  structure, in which the  ${}^2\text{F}_{5/2} \rightarrow {}^2\text{F}_{7/2}$  emission is quenched. The temperature and time dependent relaxation dynamics were studied to identify the origin of the limited QE for  $\text{Tm}^{2+}$ -doping levels below 5 mol %. An anti-correlation between the  $5\text{d}-4\text{f}$  ( ${}^3\text{H}_6, \text{t}_{2g}$ ) $_{5=3/2} \rightarrow {}^2\text{F}_{7/2}$  and  $4\text{f}-4\text{f}$   ${}^2\text{F}_{5/2} \rightarrow {}^2\text{F}_{7/2}$  emission intensities was found and rationalised by non-radiative, thermally stimulated, inter-configurational  $5\text{d}-4\text{f}$  relaxation to the emitting  ${}^2\text{F}_{5/2}$  level of  $\text{Tm}^{2+}$ . Both, the rise time of the  $4\text{f}-4\text{f}$  and the decay time of the  $5\text{d}-4\text{f}$  emission become shorter with increasing temperature. We suggest a similar non-radiative relaxation from the  $5\text{d}$  level towards the  ${}^2\text{F}_{7/2}$  ground state to limit the QE below unity. This route becomes more efficient when the  $5\text{d}$  ( ${}^3\text{H}_6, \text{t}_{2g}$ ) $_{5=3/2}$  state moves closer to the  $4\text{f}$   ${}^2\text{F}_{5/2}$  and  ${}^2\text{F}_{7/2}$  states, which is the case for the  $\text{CdCl}_2$  phase with a QE close to zero.

## 1. Introduction

$\text{Tm}^{2+}$ -doped halides are promising materials for Luminescent Solar Concentrators (LSCs). [1] LSCs should ideally exhibit broad absorption bands across the visible and ultraviolet spectral regions and an emitting centre with high quantum efficiency. These centres transfer the photon excitation energy to the semiconductor of the solar cell where an electron is excited across the band gap. Spectral overlaps between absorption bands and the emission should be absent as to prevent self-absorption losses. [2,3]

Organic dyes, such as: Coumarin CRS040 and Lumogen F Red 305, demonstrate high internal quantum efficiencies (~98%) [4], but also have a limited absorption range and suffer from significant self-absorption losses. [1,2] Quantum Dots (QDs), have lower quantum efficiencies, yet provide a means to spectrally tune the absorption and emission and hereby circumvent self-absorption losses. [2] Nevertheless, most LSC QDs, like: PbS, PbS/CdS, CdSe/CdS, still suffer from these effects. [3] For rare-earth based LSC materials, such as:

$\text{Nd}^{3+}/\text{Yb}^{3+}$ -, and  $\text{Cr}^{3+}$ -doped glasses, the absorption bands and emission are spectrally remote and hence self-absorption is absent. However, absorption ranges and quantum efficiencies are confined. Besides, the emission and the solar cell band gap share a non-perfect spectral match. [2] In comparison,  $\text{Tm}^{2+}$ -doped halides have several advantages over the aforementioned materials. They absorb up to 63% of the solar spectrum (AM 1.5) and no self-absorption occurs due to the energy difference between the  $4\text{f}-5\text{d}$  absorption and the  $4\text{f}-4\text{f}$  emission. [1] The  $\text{Tm}^{2+}$   ${}^2\text{F}_{5/2} \rightarrow {}^2\text{F}_{7/2}$  emission has negligible multi-phonon relaxation losses in low phonon energy halide lattices. The emission energy fits well with the bandgap of Copper Indium Gallium Selenide (CIGS) solar cells. An optimised  $\text{Tm}^{2+}$ -doped halide coating can appear colourless due to its broad absorption over the entire visible region. [1]  $\text{Tm}^{2+}$  luminescence in halide host materials was investigated with respect to temperature dependence and relaxation dynamics [5-9]. A detailed study of the concentration dependent emission intensity and internal quantum efficiency

is missing so far. These properties are essential for material optimisation in view of a LSC application. In this paper, we investigate SrI<sub>2</sub> samples nominally doped with 1 to 40 mol % Tm<sup>2+</sup>. The crystalline phases are characterised by powder X-ray diffraction and Rietveld refinement. The Tm<sup>2+</sup> concentrations were determined by Inductively Coupled Plasma Optically Enhanced Spectroscopy (ICP-OES) and Kubelka-Munk (K-M) absorption spectroscopy. The Tm<sup>2+</sup> luminescence and QE were investigated at room temperature. Finally, the temperature dependent relaxation dynamics was studied.

## 2. Experimental Section

### 2.1 Synthesis

A series of eight SrI<sub>2</sub>:Tm<sup>2+</sup> powder samples was synthesised by mixing SrI<sub>2</sub> (Alfa Aesar, 99.99%) with 1, 3, 5, 7, 9, 15, 25, and 40 mol % TmI<sub>2</sub> (Sigma Aldrich, 99.9%). The mixture was grinded to obtain a homogeneous powder, transferred into a silica ampoule, and attached to a vacuum/inert gas system. After evacuating and purging three times with dry nitrogen gas, the ampoule was evacuated to 10<sup>-4</sup> mbar. Then the powder was molten completely for 1-1.5 minutes using four Tecla burners. The melting points of SrI<sub>2</sub> and TmI<sub>2</sub> are 515 °C and 756 °C, respectively. The melting temperature and duration should be minimised to reduce reactions with the silica ampoule and the formation of Tm<sup>3+</sup> side products. After cooling to room temperature, the sample was removed from the ampoule and grinded. All handling of the hygroscopic and oxidation sensitive starting materials and products was done under strictly inert and dry conditions in a glovebox (MBraun, Garching, Germany) or sealed sample containers.

### 2.2 Analytical Characterisations

Powder X-ray diffraction patterns were obtained on a Philips X'pert-Pro diffractometer (Philips, Eindhoven, The Netherlands) in Bragg-Bretano geometry using CuK<sub>α</sub> radiation. The patterns were measured at room temperature from 8° to 80° 2-Theta with a resolution of 0.008°. The diffraction patterns were evaluated by the Rietveld method using the FullProf software. [10] The refined lattice parameters of the SrI<sub>2</sub> [11] and CdCl<sub>2</sub> [12] phases are summarized in Table S1 of the Supplementary Information (SI). Table S2 of the SI reports the refined atomic positions of the SrI<sub>2</sub> and CdCl<sub>2</sub> phases for samples S04 and S36, exemplarily. The Rietveld refinements of samples S04 and S36 are shown in Figures S1 and S2, respectively.

The actual Tm concentration of the samples was determined by ICP-OES measurements on a Perkin Elmer Optima 4300DV spectrometer (Perkin Elmer, Waltham Massachusetts, USA). An intensity-concentration calibration line was established from diluted standard solutions of Tm and Sr. Diffuse reflectance spectra were measured on a Bruker Vertex V80 spectrometer (Bruker, Karlsruhe, Germany) to determine the K-M absorption and to estimate the Tm<sup>2+</sup> / Tm<sup>3+</sup> ratio of the samples. The latter is based on the ratio of the integrated absorption bands of the Tm<sup>2+</sup> <sup>2</sup>F<sub>7/2</sub>→<sup>2</sup>F<sub>5/2</sub> and the Tm<sup>3+</sup> <sup>3</sup>H<sub>6</sub>→<sup>3</sup>H<sub>5</sub> transitions, as combined with their relative absorption strengths in NaI which amount to 1 and 3.4, respectively. The relative absorption strengths were established from purely Tm<sup>2+</sup>- and Tm<sup>3+</sup>-doped NaI samples; their integrated absorption band values were corrected for their ICP-OES Tm concentrations. Table 1 summarises the results of the analytical characterisations, where

**Table 1:** Analytical characterizations of the SrI<sub>2</sub>: Tm<sup>2+</sup> samples.

Sample	mol % TmI <sub>2</sub> [a]	mol % Tm ICP-OES	Tm <sup>2+</sup> / Tm <sup>3+</sup> ratio [b]	mol % Tm <sup>2+</sup> [c]	SrI <sub>2</sub> / CdCl <sub>2</sub> phases
S04	1	0.5	0.7 / 0.3	0.4	100 / 0
S06	3	0.7	0.9 / 0.1	0.6	100 / 0
S3	5	2.8	0.9 / 0.1	2.6	100 / 0
S5	7	5.5	0.9 / 0.1	4.9	100 / 0
S7	9	8.4	0.9 / 0.1	7.2	100 / 0
S12	15	14.2	0.8 / 0.2	12.0	87.4 / 12.6
S21	25	22.5	0.9 / 0.1	21.0	63.6 / 36.4
S36	40	43.2	0.8 / 0.2	36.0	37.6 / 62.4

<sup>a)</sup> nominal doping

<sup>b)</sup> from K-M absorption spectra

<sup>c)</sup> calculated from ICP-OES and K-M absorption spectra

the composition of the samples with respect to the  $\text{SrI}_2$  and  $\text{CdCl}_2$  phases is reported alongside the ICP-OES Tm concentration (column 3) and the  $\text{Tm}^{2+}/\text{Tm}^{3+}$  ratio (column 4). The samples are named after their analytical  $\text{Tm}^{2+}$  concentration (column 5).

### 2.3 Spectroscopic Measurements

Room temperature emission spectra were acquired using an Edinburgh FLS980 spectrometer (Edinburgh Instruments, Livingston, UK) with an integrating sphere, a 450 W Xenon arc lamp, and a Hamamatsu C9940-02 near infrared (NIR) photomultiplier tube (PMT) (Hamamatsu Photonics, Hamamatsu, Japan). From the same setup, absorption spectra were calculated by measuring the amount of reflected light. Highly reflecting  $\text{BaSO}_4$  and the host material  $\text{SrI}_2$  were used as reference samples. From the measured amount of emitted photons and the determined number of absorbed photons, QE values were calculated for all samples.

Temperature dependent emission and excitation spectra were acquired using a Xenon lamp coupled to a double monochromator with three gratings and a Hamamatsu C9100-13 EM-CCD or H1033A-75 NIR-PMT (Hamamatsu Photonics, Hamamatsu, Japan) that was attached to a single monochromator with three gratings to record the luminescence signals emerging from the samples. The sensitivity ranges of these detectors are 400:1150 nm and 950:1600 nm, respectively. Time resolved measurements were performed with a tuneable EKSPLA NT230 laser (EKSPLA, Vilnius, Lithuania) with a 7 ns pulse duration and 10 mJ pulse power. A DT5724F (0-2 ms) or DT5730 (0-40 ms) CAEN digitiser (CAEN, Viareggio, Italy) measured the signal from a H1033A-75 NIR-PMT or a Hamamatsu R7600U-20HV-800V PMT (Hamamatsu Photonics, Hamamatsu, Japan). Signals from 1000 laser pulses were cumulated for each decay spectrum. The samples were heated and cooled by aid of an APD Cryogenic Helium cooler (APD Cryogenics, Allentown Pennsylvania, USA) and Lakeshore temperature controller (Lakeshore Cryotronics, Westerville Ohio, USA).

During all measurements, sealed containments protected the samples against moisture and oxidation reactions. Similar sample holders were described by Rogers et al. [13].

## 3. Results and Discussion

### 3.1 Sample Characterisation

The lattice parameters and phase composition of the samples were determined by X-ray diffraction. The lattice parameters are summarized in Table S1 of the SI. The Rietveld refinements reveal a single-phase  $\text{SrI}_2$  structure [11] for  $\text{SrI}_2$ : Tm samples with Tm contents below 8 mol %. A Rietveld fit of sample S04 is shown in Figure S1 of the SI. The sample names refer to their analytical  $\text{Tm}^{2+}$  concentration given in Table 1 (column 5).

The lattice parameters and molar volume slightly decrease with increasing Tm content, which is in good agreement with the smaller ionic radius of  $\text{Tm}^{2+}$  (1.09 Å for Coordination Number (CN) 7) compared to  $\text{Sr}^{2+}$  (1.21 Å for CN 7) [14]. The  $\text{Tm}^{2+}$  ions replace  $\text{Sr}^{2+}$  on regular lattice sites of the  $\text{SrI}_2$  crystal structure. The refined atomic positions for sample S04 are shown in Table S2 of the SI. They agree well with the published crystal structure of  $\text{SrI}_2$  [11].  $\text{SrI}_2$  crystallises in the orthorhombic space group  $\text{Pbca}$ . The structure has one  $\text{Sr}^{2+}$  site (8c) with sevenfold coordination and  $\text{C}_1$  point symmetry, see Figure 1a.

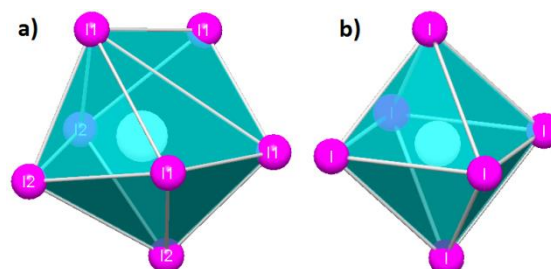


**Figure 1:** (a) Seven-fold coordination of  $\text{Tm}^{2+}$  by  $\text{I}^-$  in the  $\text{SrI}_2$  phase and (b) six-fold coordination in the  $\text{CdCl}_2$  phase.

For higher  $\text{Tm}^{2+}$  concentrations the diffraction patterns reveal the presence of a second phase with  $\text{CdCl}_2$  crystal structure [12]. A Rietveld fit of sample S36 is shown in Figure S2 and the atomic positions in Table S2 of the SI.  $\text{CdCl}_2$  crystallizes in the rhombohedral space group  $\text{R}\bar{3}\text{m}$ . The structure has one cation site (3a) with sixfold coordination and  $\text{D}_{3d}$  point symmetry, see Figure 1b. The fraction of the  $\text{CdCl}_2$  phase amounts to 13, 36, and 62 mol % with increasing  $\text{Tm}^{2+}$ -doping of 12, 21, and 36 mol %, respectively, see Table 1.

The  $\text{Tm}^{2+}$  concentration in all samples was determined by ICP-OES and K-M absorption measurements. The analytical  $\text{Tm}^{2+}$  concentrations

are reasonably close to the nominal values according to the  $\text{SrI}_2/\text{TmI}_2$  molar ratio of the starting materials, see Table 1.

The K-M absorption spectra are shown in Figure 2. From these spectra the  $\text{Tm}^{2+}/\text{Tm}^{3+}$  ratio of the samples was determined. The spectra are normalised to the broad  $\text{Tm}^{2+}$  4f-5d absorption band at 650 nm and vertically shifted by 0.2 relative to each other. The 4f-4f absorption bands of  $\text{Tm}^{2+}$   ${}^2\text{F}_{7/2} \rightarrow {}^2\text{F}_{5/2}$  at 1140 nm and  $\text{Tm}^{3+}$   ${}^3\text{H}_6 \rightarrow {}^3\text{H}_5$  at 1230 nm, were integrated, normalised to their respective absorption in NaI, and multiplied by the Tm concentration from the ICP-OES. We refer to Figure 9 below for a  $\text{Tm}^{2+}$  energy level scheme and term symbols.

The coordination of the  $\text{Tm}^{2+}$  ions strongly affects the crystal field splitting of the 5d state. The higher symmetry and shorter Tm-I distances in the sixfold coordination of the  $\text{CdCl}_2$  phase give rise to a stronger crystal field splitting, which shifts its lowest 5d level beyond that of the  $\text{SrI}_2$  phase. This additional low energy 5d band becomes visible at 740 nm in the absorption spectra of Figure 2. It is weak for sample S7 and increases with the fraction of the  $\text{CdCl}_2$  phase towards sample S36.

is immediately observed, the 5d absorption band related to the  $\text{CdCl}_2$  phase is absent in the excitation spectra. This illustrates that the  $\text{Tm}^{2+}$  ions that occupy the Sr-sites in this phase have very little to no contribution to the  ${}^2\text{F}_{5/2} \rightarrow {}^2\text{F}_{7/2}$  emission at room temperature.

Furthermore, the overall shape of the excitation spectra seems to change for increasing  $\text{Tm}^{2+}$ -doping concentrations. Most notably, the excitation bands located between 220-400nm undergo a drop in intensity as the doping concentration increases from 3 to 5 mol %. In addition to that, the excitation bands located between 550-750 nm also seem to undergo a change of shape as the  $\text{Tm}^{2+}$  concentration increases from 12 to 36 mol %; which is the interval where the  $\text{CdCl}_2$  phase intensifies. A possible explanation for this could be that as the  $\text{Tm}^{2+}$  concentration is increased, the average distance between the  $\text{Tm}^{2+}$  ions decreases; resulting in an alteration in the local surroundings of these ions. As a consequence, the affined excitation bands are shifted leading to a change in local spectra intensity.

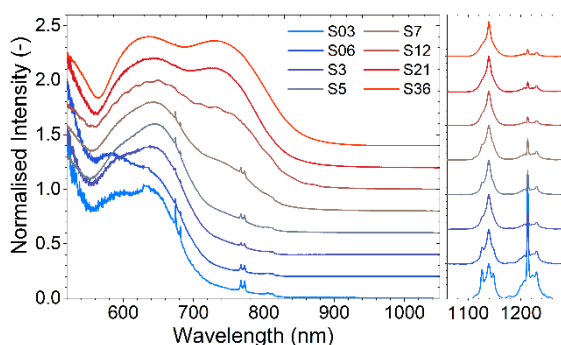


**Figure 2:** Kubelka-Munk absorption spectra of  $\text{SrI}_2:\text{Tm}$  samples. Sample names refer to Table 1. The spectra are normalised to the broad  $\text{Tm}^{2+}$  4f-5d absorption band at 650 nm and vertically shifted (by 0.2) relative to each other. (right) 4f-4f absorption peaks of  $\text{Tm}^{2+}$   ${}^2\text{F}_{7/2} \rightarrow {}^2\text{F}_{5/2}$  at 1140 nm and  $\text{Tm}^{3+}$   ${}^3\text{H}_6 \rightarrow {}^3\text{H}_5$  at 1230 nm.

### 3.2 Concentration Dependent Luminescence

With their  $\text{Tm}^{2+}$ -doping concentrations estimated and their structural properties examined, the room temperature luminescence characteristics of the samples are explored. Figure 3 shows the excitation spectra of the different samples monitoring the  $\text{Tm}^{2+}$   ${}^2\text{F}_{5/2} \rightarrow {}^2\text{F}_{7/2}$  emission. For convenience, the K-M absorption spectra are plotted in this figure, too. As

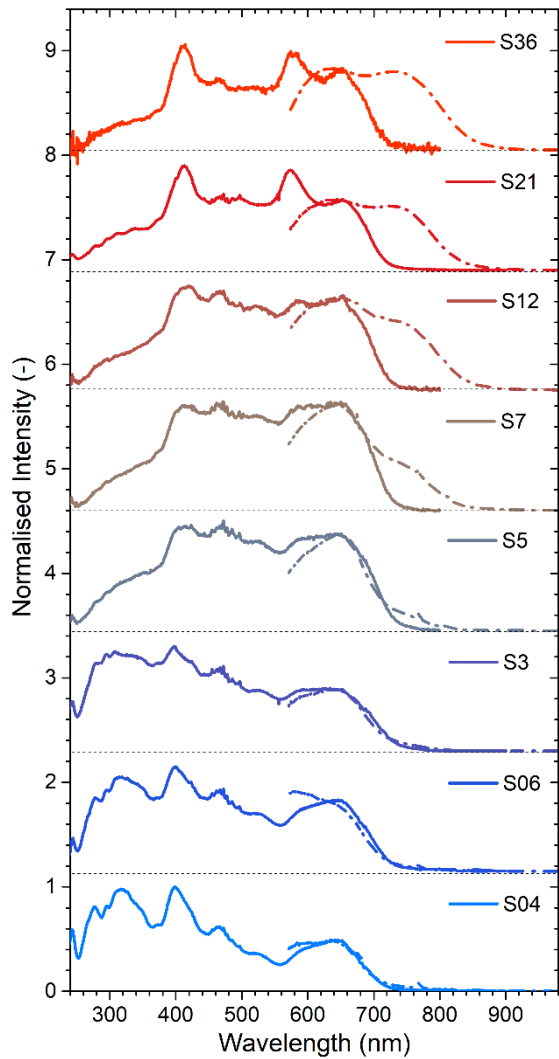


**Figure 3:** Excitation (full line) and K-M absorption (dotted line) spectra of the  $\text{SrI}_2:\text{Tm}^{2+}$  samples at room temperature. The excitation spectra were recorded for the  $\text{Tm}^{2+} \ ^2\text{F}_{5/2} \rightarrow \ ^2\text{F}_{7/2}$  transition at 1140 nm and are normalized to the band at 410 nm. The sample names refer to Table 1.

After a selective photoexcitation at 655 nm, the absorption and emission properties of the samples were examined. Figure 4a shows that the reflectance of the samples decreases steadily as the  $\text{Tm}^{2+}$  concentration is increased from 0.4 to 3 mol %; indicating an increased absorption contribution of the  $\text{SrI}_2:\text{Tm}^{2+}$  luminescence centres. As the  $\text{Tm}^{2+}$ -doping concentration reaches a value of 12 mol % the reflectance, and hence also the absorption, of the samples slowly saturates.

In addition, Figure 4b shows that as the  $\text{Tm}^{2+}$ -doping concentration is increased from 0.4 to 3 mol %, the luminescence intensity of the  $\text{Tm}^{2+} \ ^2\text{F}_{5/2} \rightarrow \ ^2\text{F}_{7/2}$  emission also increases. However, upon reaching a

doping concentration of 5 mol %, it decreases again as shown in panel c.

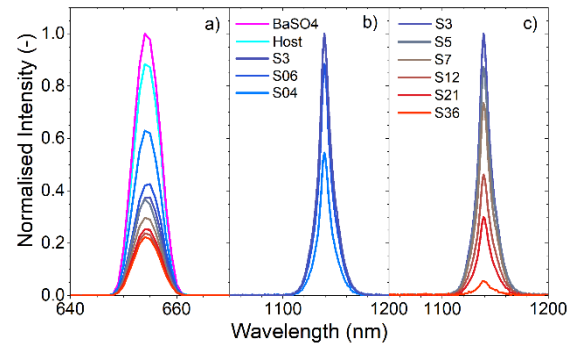


**Figure 4:** (a) Reflectance spectra of the samples and  $\text{SrI}_2$  (host) relative to  $\text{BaSO}_4$ . (b,c)  $\text{Tm}^{2+} \ ^2\text{F}_{5/2} \rightarrow \ ^2\text{F}_{7/2}$  emission spectra. The sample names refer to Table 1.

In order to better determine the absorption contribution of the  $\text{SrI}_2:\text{Tm}^{2+}$  luminescence centres to the overall absorption of the samples, the reflectance of pure  $\text{SrI}_2$  powder (Alfa Aeser, 99.99%) was compared to purely reflecting  $\text{BaSO}_4$  (Sigma Aldrich, 99.99%) at the selected wavelength of photoexcitation. The  $\text{SrI}_2$  host absorption contribution to the samples was hereby estimated to be 10-13%. The host corrected relative values for the absorption and integrated emission were used to determine the internal quantum efficiency of the samples. For each specific sample, these quantities are plotted versus their estimated  $\text{Tm}^{2+}$  concentration in Figure 5, whereas Table S3 in the SI provides a summary overview. As is perceived, the red integrated emission curve qualitatively follows from the product of the green quantum efficiency curve and the blue relative absorption curve.

As the  $\text{Tm}^{2+}$ -doping concentration increases from 0.6 up to 5 mol %, the relative absorption rapidly increases to a value of 59%. Meanwhile, the QE remains virtually constant at the a value of 52%. The luminescence intensity is therefore controlled by the absorption. For  $\text{Tm}^{2+}$  concentrations higher than about 5 mol %, the QE starts to decrease while the increase in absorption becomes less brisk. As a result, the luminescence intensity reaches an optimum at a  $\text{Tm}^{2+}$  concentration of 3 mol % after which it starts to follow the QE.

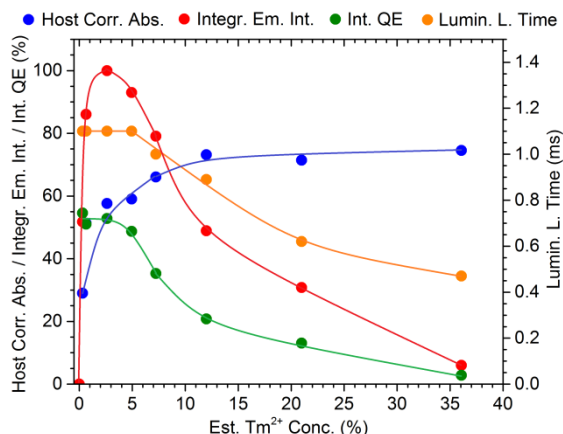


**Figure 5:** The absorption relative to the pure host, normalised integrated  ${}^2F_{5/2} \rightarrow {}^2F_{7/2}$  emission intensity, internal quantum efficiency, and the  ${}^2F_{5/2} \rightarrow {}^2F_{7/2}$  emission lifetimes of the samples as plotted versus their estimated  $Tm^{2+}$  concentrations.

The luminescence lifetime of the  $Tm^{2+} {}^2F_{5/2} \rightarrow {}^2F_{7/2}$  emission, indicated by the orange curve, was also investigated for all eight samples. The corresponding decay curves are plotted in Figure 6 and reveal that the slope of the decay curves stays constant up to a concentration of 5 mol %. This implies that the luminescence lifetime, also presented in Table S3, remains constant. For higher  $Tm^{2+}$ -doping concentrations, the tail part of the decay curves can be approximated by a single exponential with luminescence lifetimes steadily decreasing.

Since the luminescence lifetime is proportional to the quantum efficiency, one would expect an equal decline over concentration. The QE declines by a factor of almost 20, from 55% at the lowest  $Tm^{2+}$  concentration to 3% at a  $Tm^{2+}$  concentration of 36 mol %. The decay time however only drops by a factor of 2. This apparent discrepancy can be explained by the presence of the  $CdCl_2$  phase at higher  $Tm^{2+}$  concentrations. As Table 1 reveals, sample S12 already contains a large fraction of the  $CdCl_2$  phase. The  $Tm^{2+}$ -doping ions that occupy the Sr-sites in this phase have a significant impact on the absorption, yet there is only a very small contribution to the  ${}^2F_{5/2} \rightarrow {}^2F_{7/2}$  emission intensity. The non-equivalent decrease can hence be explained by the fact that the QE measurements are based on the contributions of both structural phases; whereas the luminescence lifetime measurements only involve the contributions of the  $Tm^{2+}$  ions that are present in the regular  $SrI_2$  phase.

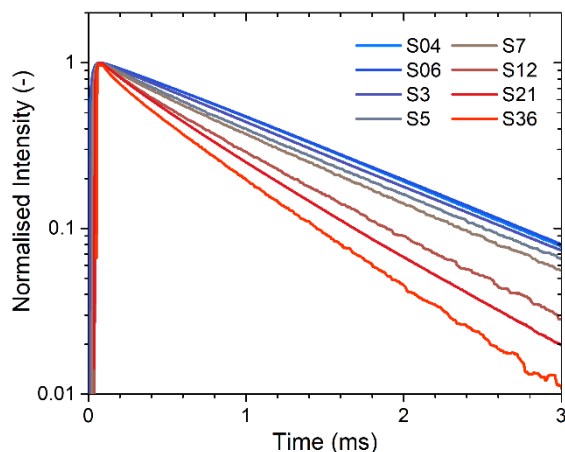


**Figure 6:** Normalised decay curves of the  $Tm^{2+} {}^2F_{5/2} \rightarrow {}^2F_{7/2}$  emission under 410 nm pulsed laser excitation at room temperature. The intensity is plotted on a log-scale. The sample names refer to Table 1.

Upon reaching a  $Tm^{2+}$ -doping concentration of 36 mol %, the highest in the sample series, the internal quantum efficiency has decreased to a mere 3%, while the integrated emission intensity has reduced to 6%. In addition, the luminescence lifetime reaches a value of 0.47 ms. The host corrected absorption has become constant with concentration and attains at 75%.

Since all measurements were performed at the same temperature, thermal quenching mechanisms cannot be responsible for the decrease in the luminescence lifetime and emission intensity. Since the  $Tm^{2+}$ -doping concentration is the only parameter varied, the quenching can be attributed to concentration quenching, where the  $Tm^{2+}$  concentration of about 5 mol % forms the critical concentration.

### 3.3 Temperature Dependent Luminescence

As became apparent in the previous section, the QE of the samples is limited to 53% and does not reach a full 100%. This observation has incited us to investigate the temperature dependent relaxation dynamics of three selected samples. Sample S3 contains only the regular  $SrI_2$  phase and its  $Tm^{2+}$ -doping concentration lies below the critical value where concentration quenching is encountered. Sample S7 also contains the regular  $SrI_2$  phase, but lies slightly above the critical concentration. Sample S21 contains a substantial amount of the  $CdCl_2$  phase aside the  $SrI_2$  phase and its  $Tm^{2+}$  content ranges far above the critical concentration.

### Emission Classification

Figure 7 shows the emission spectra of the three samples as photoexcited at 410 nm and for the temperatures of 20 K and 300 K. Up to four distinct  $\text{Tm}^{2+}$  emissions are observed. The emissions are labelled A to C in analogy to the work of Grimm et al. and our previous article [5-9].

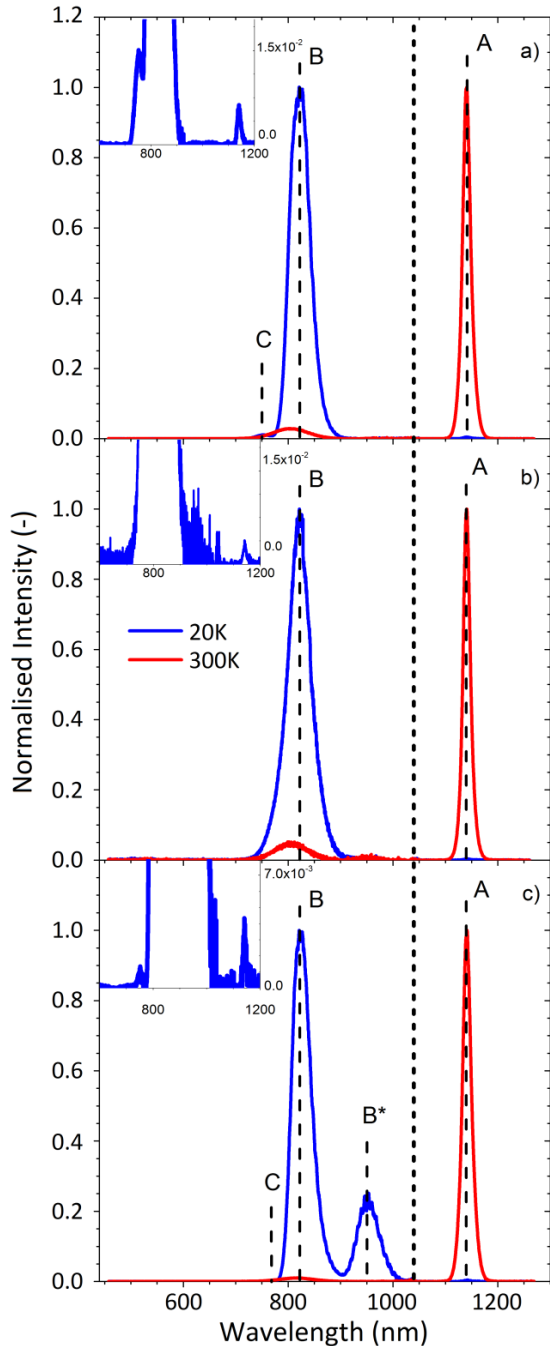


**Figure 7:** Emission spectra of samples S3 (a), S7 (b), and S21 (c) under 410 nm excitation at 20 K and 300 K. The dashed line at 1040 nm separates the CCD and NIR-PMT detector ranges with different sensitivities. The CCD spectra are normalised on emission B at 20 K, the NIR-

PMT spectra on emission A at 300 K. The sample names refer to Table 1 and emission labels to Figure 9.

For all samples, 5d-4f emission B appears to be very intense at low temperature; while 4f-4f emission A is most dominant at room temperature. Furthermore, 5d-4f emission C only appears in samples S3 and S21; while for the latter sample an additional 5d-4f emission is observed which is labelled as B\*. Since all emissions are present in sample S21, excitation spectra were recorded for each emission peak and are displayed in Figure 8. The excitation spectrum of emission B\* deviates distinctively from the others. The observed bands are shown in an energy level diagram in Figure 9.

For  $\text{SrI}_2:\text{Yb}^{2+}$  the lowest energy 4f-5d spin-forbidden excitation band is located at 418 nm. [15] Using the constant, material independent energy difference of 1.2 eV between the 5d state energies of  $\text{Yb}^{2+}$  and  $\text{Tm}^{2+}$ , as discussed by Dorenbos et al. [16], the lowest energy spin-forbidden excitation band of  $\text{Tm}^{2+}$  in  $\text{SrI}_2$  should be located at around 728 nm. The excitation spectrum of emission B in Figure 8 shows indeed such a band located at around 724 nm. The lowest energy spin-allowed 4f-5d excitation band for  $\text{SrI}_2:\text{Yb}^{2+}$  is observed at 390 nm. For  $\text{SrI}_2:\text{Tm}^{2+}$  its location is therefore predicted at around 651 nm. [15] Figure 8 shows a band at 654 nm in the excitation spectra of emissions A, B, and C. The excitation spectrum of emission B\*, does not match any of those bands. It shows a band at around 740 nm which resembles the K-M absorption spectra shown in Figure 2. It can therefore be concluded that emission B\* emerges from the  $\text{Tm}^{2+}$  ions in the  $\text{CdCl}_2$  phase.

Now that the lowest energy 5d-4f excitation bands have been identified, Stokes shift values can be used to classify the emissions. The Stokes shift of the  $\text{Yb}^{2+}$   $4f^{13}[^2F_{5/2}]5d \rightarrow 4f^{14}$  spin-allowed emission in  $\text{SrI}_2$  amounts to 0.21 eV. [15] When adding this value to the  $\text{Tm}^{2+}$  5d-4f emissions in  $\text{SrI}_2$ , a good agreement is achieved with the excitation bands in Figure 8. Emission B in sample S21 is observed at 823 nm. Subtracting the Stokes shift energy, an excitation band should be expected near 720 nm.

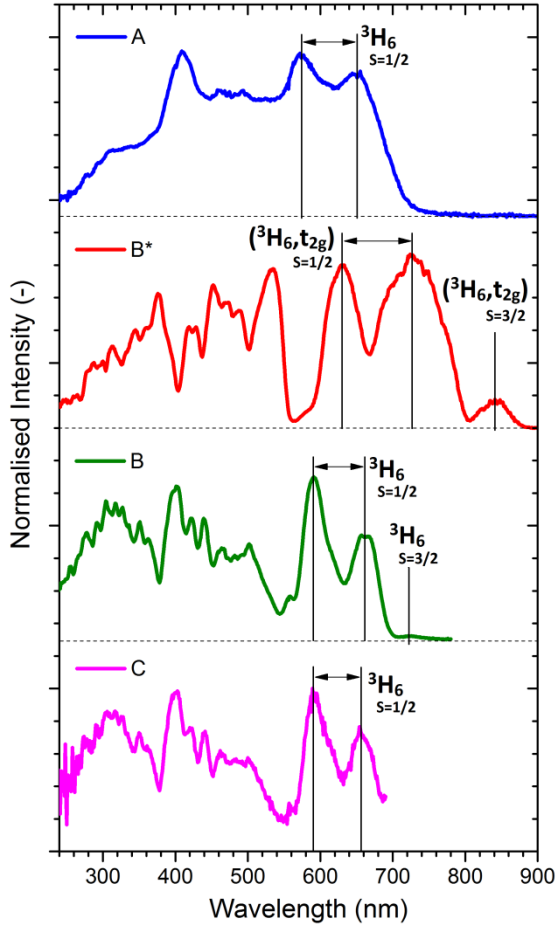


**Figure 8:** Excitation spectra of the four distinct  $Tm^{2+}$  emissions in sample S36. The spectra are normalised on the band between 560-630 nm and recorded at 20 K (B, B\*, C) or 300 K (A). Emission labels refer to Figure 9.

The excitation spectrum shows the presence of a weak band at 724 nm. Therefore, emission B can be classified as the transition from the  $(^3H_6)_{S=3/2}$  spin-forbidden 5d level towards the  $^2F_{7/2}$  4f-ground state, see Figure 9. Similarly emission C corresponds to an excitation band located at 665nm, which represents the spin-allowed  $(^3H_6)_{S=1/2}$  5d level. Consequently, emission C is related to the  $(^3H_6)_{S=1/2} \rightarrow ^2F_{7/2}$

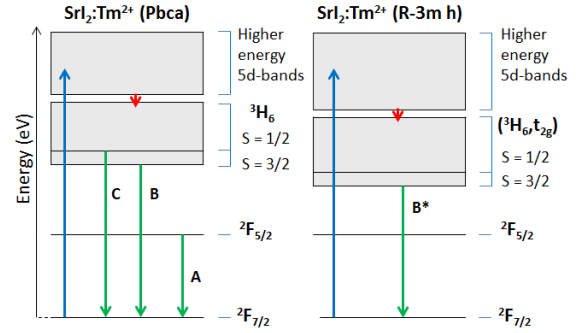


**Figure 9:** Energy level diagram of  $Sr_{12}:Tm^{2+}$  in the  $Sr_{12}$  (Pbca) and  $CdCl_2$  (R-3m h) phases. After excitation at 410 nm (blue arrow) four distinct emissions (green arrows) are observed at 20 K. The emission labels refer to Table 3.

transition. The decay time of emission B at 20 K is provided in Table 3; it is in the order of a few hundred microseconds. In contrast, emission C decays in a few hundred nanoseconds which is three orders of magnitude faster. This difference in decay times is caused by the spin-forbidden and spin-allowed nature of the respective transition. Emission A is located at 1140 nm and represents the  $Tm^{2+} \ ^2F_{5/2} \rightarrow ^2F_{7/2}$  4f emission. Its relatively slow decay time of 618  $\mu s$  reflects the parity forbidden nature of this emission.

Upon adding the Stokes shift energy value to emission B\*, an excitation band should be present at 820 nm. Such a band can only be observed in the excitation spectrum of emission B\* itself. It is located close to 841 nm and assigned to the  $(^3H_6, t_{2g})_{S=3/2}$  spin-forbidden 5d level of the  $Tm^{2+}$  ions in the  $CdCl_2$  phase. Hence, the emission is associated with the  $(^3H_6, t_{2g})_{S=3/2} \rightarrow ^2F_{7/2}$  transition.

**Table 3:** Overview on the four distinct  $Tm^{2+}$  emissions observed in samples S3, S7, and S21.

Sample	Emission	Transition	Wavelength (20K) [nm]	Energy (20K) [eV]	Decay Time(s)
S3	C	$(^3H_6)_{S=1/2} \rightarrow ^2F_{7/2}$	755	1.64	310 ns, 765 ns (20K)
	B	$(^3H_6)_{S=3/2} \rightarrow ^2F_{7/2}$	822	1.51	260 $\mu s$ (20K)
	A	$^2F_{5/2} \rightarrow ^2F_{7/2}$	1141	1.09	1.10 ms (300K)
S7	B	$(^3H_6)_{S=3/2} \rightarrow ^2F_{7/2}$	821	1.51	265 $\mu s$ (20k)
	A	$^2F_{5/2} \rightarrow ^2F_{7/2}$	1141	1.09	1.03 ms (300K)
	C	$(^3H_6)_{S=1/2} \rightarrow ^2F_{7/2}$	752	1.65	210 ns, 635 ns (20K)
S21	B	$(^3H_6)_{S=3/2} \rightarrow ^2F_{7/2}$	823	1.51	260 $\mu s$ (20K)
	B*	$(^3H_6)_{S=3/2} \rightarrow ^2F_{7/2}$	954	1.30	80 $\mu s$ , 220 $\mu s$ (20K)
	A	$^2F_{5/2} \rightarrow ^2F_{7/2}$	1142	1.09	618 $\mu s$ (300K)

### Temperature Dependence of Emission Intensities

At a temperature of 20 K all four observed emissions are present. The temperature plots in Figure 10 show that, for all three samples, emission B is most intense at 20 K. As the temperature increases to 100 K, its luminescence intensity stays relatively constant, see also Figure 11. Above 100 K the intensity decreases rapidly and the emission starts to quench. An Arrhenius analysis shows that the thermal activation energies related to the quenching process amount to 203, 104, and 225 meV for samples S3, S7, and S21 respectively. The observations in the emission intensity are supported by trends in the luminescence lifetimes of emission B. At 20 K, the lifetime of this emission amounts to 265  $\mu$ s for sample S7. For temperatures up to 100 K, the decay curves remain parallel to each other and hence the luminescence lifetime remains constant, as illustrated in Figure 12c. Above 100 K, the decay curves contract and the luminescence lifetime reaches a value of 11  $\mu$ s at 300 K. Similar trends were observed in the luminescence lifetime spectra of samples S3 and S21, where the lifetime is around 260  $\mu$ s at 20 K and 9  $\mu$ s and 23  $\mu$ s at 300 K respectively.

Emission A is already weakly present at the lowest studied temperature of 20 K. The temperature plots in Figure 10 reveal that from 100 K onwards, the intensity of emission A undergoes a drastic increase. This behaviour is precisely anti-correlated to that of emission B. The decay curves of emission A remain parallel over the entire temperature range of 20-300 K, indicating a constant luminescence lifetime. However, already at 20 K the decay curves in Figure 12a display a small rise time phenomena. As the temperature is increased to 100 K, the rise time duration changes from 22  $\mu$ s to 30  $\mu$ s; suggesting that the luminescence feeding process slows down. This process allows it to explain the presence of the 4f-4f emission A at 20 K. Since the energy gap between the  $(^3H_6)_{5=3/2}$  and  $^2F_{5/2}$  levels is around 417 meV, its origin might possibly be related to the quenching of emission B via highly efficient multiphonon relaxation. However, this would decrease the luminescence of emission B at low temperature, which is clearly not observed in Figure 11. Alternatively, the VRBE diagram of SrI<sub>2</sub>, as established by Alekhin et al. [17], reveals that the Tm<sup>2+</sup> 5d band used for photoexcitation is located in

the conduction band. The weak presence of emission A at low temperatures could then also be explained by a feeding mechanism via conduction band states. A similar mechanism has been opted and described in our previous article. [9] When the temperature increases further from 150 K to 300 K, the rise time duration shortens from 30  $\mu$ s to 13  $\mu$ s; indicating a faster feeding. This occurs in the temperature range in which emission B quenches, something that was previously also encountered for NaBr:Tm<sup>2+</sup>. [9] The quenching mechanism of emission B can then most likely be attributed to interband crossing.

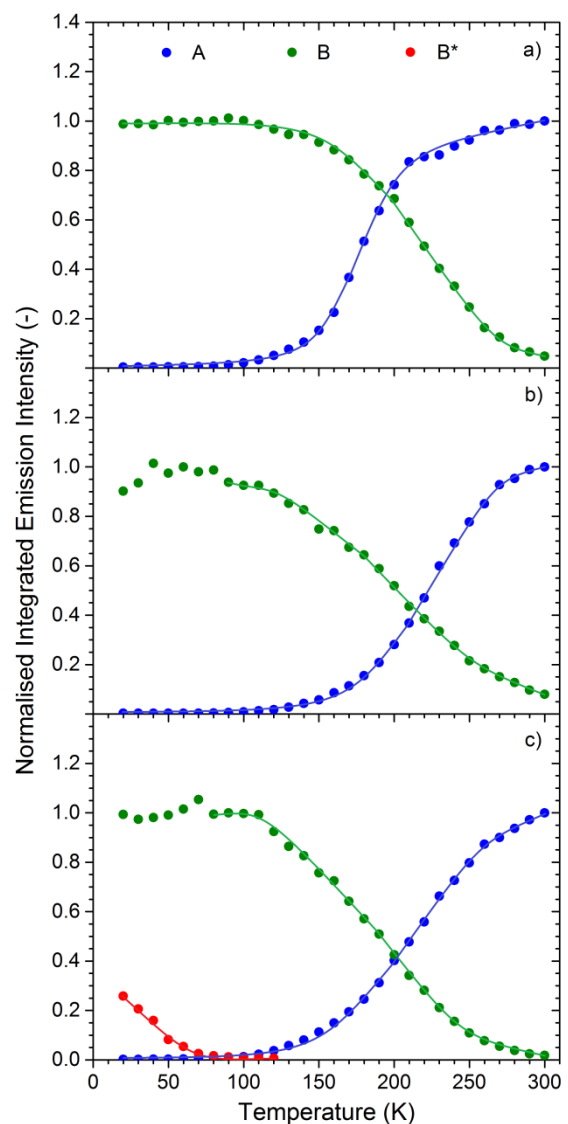


**Figure 10:** Temperature dependence of the normalised integrated Tm<sup>2+</sup> emission intensity of emissions A, B, and B\* for samples S3 (a), S7 (b), and S21 (c). Samples were excited at 410 nm. Sample names refer to Table 1 and emission labels to Table 3. The solid lines serve as a guide to the eye.

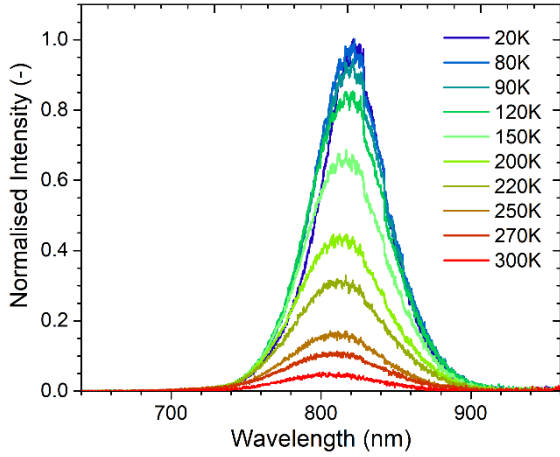


**Figure 11:** Temperature dependence of the  $\text{Tm}^{2+}$  ( ${}^3\text{H}_6, t_{2g}$ ) $_{S=3/2} \rightarrow {}^2\text{F}_{7/2}$  emission B of sample S7 under 410 nm excitation at 20 K. The spectra are normalised to 20 K.

Emission C is only present in samples S3 and S21 and the temperature dependent emission spectra in Figure S3 in the SI reveal that it is most intense at 20 K. As the temperature increases its intensity decreases and it starts to undergo quenching; having quenched completely at 100 K. Since the energy gap between the ( ${}^3\text{H}_6$ ) $_{S=1/2}$  and ( ${}^3\text{H}_6$ ) $_{S=3/2}$  levels is close to 140 meV, the quenching can most likely be associated with multi-phonon relaxation.

Emission B\* emerges from the  $\text{Tm}^{2+}$  ions in the  $\text{CdCl}_2$  phase and originates from the ( ${}^3\text{H}_6, t_{2g}$ ) $_{S=3/2}$  level. It is only present in sample S21 and Figures 10 and S4 show that its luminescence intensity already starts to decrease rapidly at 20 K. At 100-120 K, the emission is quenched completely. The energy difference between the ( ${}^3\text{H}_6, t_{2g}$ ) $_{S=3/2}$  and  ${}^2\text{F}_{5/2}$  levels is around 384 meV and hence the quenching can likely be attributed to multi-phonon relaxation.

Room temperature excitation into the ( ${}^3\text{H}_6, t_{2g}$ ) $_{S=3/2}$  level at 840 nm reveals a very weak  ${}^2\text{F}_{5/2} \rightarrow {}^2\text{F}_{7/2}$  emission that is not there at 20 K, see Figure S5 in the SI. At this excitation wavelength the  $\text{Tm}^{2+}$  ions in the regular  $\text{SrI}_2$  phase are not excited and the observed  ${}^2\text{F}_{5/2} \rightarrow {}^2\text{F}_{7/2}$  emission can only emerge from the  $\text{Tm}^{2+}$  ions in the  $\text{CdCl}_2$  phase. However, the perceived  ${}^2\text{F}_{5/2} \rightarrow {}^2\text{F}_{7/2}$  emission at 300 K is much weaker than emission B\* at 20 K, which could indicate the presence of a quenching route towards the ground state.

#### 4. Conclusions

For the  $\text{SrI}_2\text{-TmI}_2$  system, the QE of the  ${}^2\text{F}_{5/2} \rightarrow {}^2\text{F}_{7/2}$  emission attains a value of over 50%. As the  $\text{Tm}^{2+}$ -doping concentration reaches the critical value of 5 mol %, the QE starts to decrease due to concentration quenching effects and the appearance of a second structural phase that has a profound contribution to the absorption yet a negligible effect on the  ${}^2\text{F}_{5/2} \rightarrow {}^2\text{F}_{7/2}$  emission. Since the QE partly determines the overall efficiency of the LSC application, a  $\text{Tm}^{2+}$ -doping concentration below the critical value is therefore desired. In an attempt to explain why the QE value is bounded to 50%, the temperature dependent relaxation dynamics were investigated. In resemblance to other  $\text{Tm}^{2+}$ -doped halide studies, the ( ${}^3\text{H}_6$ ) $_{S=3/2} \rightarrow {}^2\text{F}_{7/2}$  emission quenches over temperature and feeds the  ${}^2\text{F}_{5/2} \rightarrow {}^2\text{F}_{7/2}$  emission. A rise time phenomena reveals that the related quenching mechanism is most likely interband crossing. Nevertheless, there is no clear indication why the QE is limited to 50%. It is suggested that there might be a non-radiative route

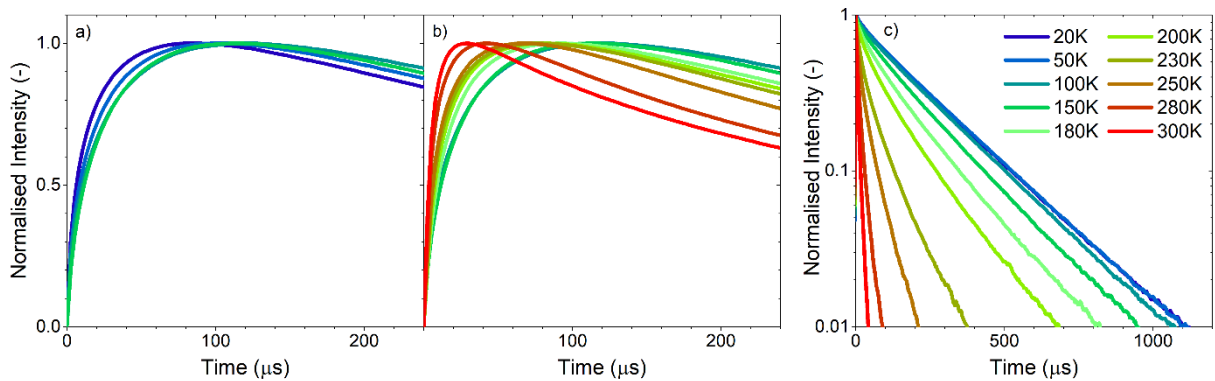


**Figure 12:** The time resolved spectra showing the rise time phenomena as present in the decay curves of  ${}^2\text{F}_{5/2} \rightarrow {}^2\text{F}_{5/2}$  emission A (ab) and the decay curves of ( ${}^3\text{H}_6, t_{2g}$ ) $_{S=3/2} \rightarrow {}^2\text{F}_{7/2}$  emission B (c) in sample S7 at different temperatures. The time-resolved spectra were acquired using pulsed laser excitation at 410 nm.

from the  $(^3H_6, t_{2g})_{S=3/2}$  level towards the  $^2F_{7/2}$  ground state possibly via an additional interband crossing between the two levels. It is therefore recommended to investigate this possibility further by analysis of the sensitivity corrected relative  $(^3H_6, t_{2g})_{S=3/2} \rightarrow ^2F_{7/2}$  and  $^2F_{5/2} \rightarrow ^2F_{7/2}$  emission intensities, instead of the normalised values as presented in Figures 7 and 10, and in combination with theoretical modelling via rate equations.

## 5. Acknowledgement

This research was financially supported by the Nederlandse Organisatie voor Wetenschappelijk onderzoek (NWO) as part of the LumiCon proposal. The authors would like to thank D.A. Biner (Bern University) for the synthesis of a part of the  $TmI_2$  starting material, J.T.M. de Haas (TU Delft) for experimental support with the photoluminescence measurements, and B.E. Terpstra (TU Delft) for experimental support with ICP-OES measurements.

## 6. References

- [1] O.M. ten Kate, K.W. Krämer, E. Van der Kolk, Efficient luminescent solar concentrators based on self-absorption free,  $Tm^{2+}$  doped halides, *Sol. Energy Mater Sol. Cells* 115-120 (2015) 140.
- [2] M.G. Debije, P.P.C. Verbunt, Thirty Years of Luminescent Solar Concentrator Research: Solar Energy for the Built Environment, *Adv. Energy Mater.* (2011) 2.
- [3] F. Meinardi, F. Bruni, S. Brovelli, Luminescent solar concentrators for building-integrated photovoltaics, *Nat. Rev. Mater.* (2017) 2 17072
- [4] W.G.J.H.M. van Sark, K.W.J. Barnham, L.H. Slooff, A.J. Chatten, A. Büchtemann, A. Meyer, S.J. McCormack, R. Koole, D.J. Farrell, R. Bose, E.E. Bende, A.R. Burgers, T. Budel, J. Quilitz, M. Kennedy, T. Meyer, C. De Mello Donegá, A. Meijerink, D. Vanmaekelbergh, Luminescent Solar Concentrators - A review of recent results, *Opt. Express* (2008) 16 26 21773
- [5] J. Grimm, H.U. Güdel, Five different types of spontaneous emission simultaneously observed in  $Tm^{2+}$  doped  $CsCaBr_3$ , *Chemical Physics Letters* 40–43 (2005) 404
- [6] J. Grimm, O.S. Wenger, K.W. Krämer, H.U. Güdel, 4f-4f and 4f-5d excited states and luminescence properties of  $Tm^{2+}$ -doped  $CaF_2$ ,  $CaCl_2$ ,  $SrCl_2$ ,  $BaCl_2$ , *J. Phys. Chem. B* 101-105 (2006) 110.
- [7] J. Grimm, J.F. Suyver, G. Carver, H. U. Güdel, Light-Emission and Excited-State Dynamics in  $Tm^{2+}$  Doped  $CsCaI_3$ ,  $CsCaBr_3$ , and  $CsCaCl_3$ , *J. Phys. Chem. B* 2093-2101 (2006) 110.
- [8] E. Beurer, J. Grimm, P. Gerner, H.U. Güdel, Absorption, Light Emission, and Upconversion Properties of  $Tm^{2+}$ -doped  $CsCaI_3$  and  $RbCaI_3$ , *Inorg. Chem.* 9901-9906 (2006) 45.
- [9] M.P. Plokker, E. van der Kolk, Temperature dependent relaxation dynamics of luminescent  $NaX:Tm^{2+}$  ( $X=Cl, Br, I$ ), *J. Lumin.* (2019) 216.
- [10] J. Rodriguez-Carvajal, program FullProf.2k, version 5.2, July-2011, Institute Laue Langevin.
- [11] S.A. Hodorowicz, H.A. Eick, An X-ray diffraction study of the  $SrBr_{1-x}I_x$  system, *J. Solid State Chem.* 313-320 (1983) 46.
- [12] D.E. Partin and M.J. O'Keefe, The structures and crystal chemistry of magnesium chloride and cadmium chloride, *Solid State Chem.* 176-183 (1991) 95.
- [13] E. Rogers, P. Dorenbos, J.T.M. de Haas, E. van der Kolk, Experimental study of the  $4f^n \rightarrow 4f^n$  and  $4f^n \rightarrow 4f^{n-1}5d^1$  transitions of the lanthanide diiodides  $LnI_2$  ( $Ln = Nd, Sm, Eu, Dy, Tm, Yb$ ), *J. Phys.: Condens. Matter* (2012) 24.
- [14] R.D. Shannon, Revised Effective Ionic Radii and Systematic Studies of Interatomic Distances in Halides and Chalcogenides, *Acta Crystallogr.* A32 (1976) 751.
- [15] M.S. Alekhin, D.A. Biner, K.W. Kraemer, P. Dorenbos, Optical and scintillation properties of  $SrI_2:Yb^{2+}$ , *Opt. Mater.* 382-386 (2014) 37.
- [16] P. Dorenbos, Energy of the first  $4f_7 \rightarrow 4f_65d$  transition of  $Eu^{2+}$  in inorganic compounds, *J. Lumin.* 239-260 (2003) 104.
- [17] M.S. Alekhin, R.H.P. Awater, D.A. Biner, K.W. Kraemer, J.T.M. de Haas, P. Dorenbos, Luminescence and spectroscopic properties of  $Sm^{2+}$  and  $Er^{3+}$  doped  $SrI_2$ , *J. Lumin.* 347-351 (2015) 167.